



# Ions in the Thermosphere of Exoplanets: Observable Constraints Revealed by Innovative Laboratory Experiments

Jérémy Bourgalais<sup>1</sup> , Nathalie Carrasco<sup>1</sup> , Quentin Changeat<sup>2</sup> , Olivia Venot<sup>3</sup> , Lora Jovanović<sup>1</sup>, Pascal Pernot<sup>4</sup>,  
Jonathan Tennyson<sup>2</sup> , Katy L. Chubb<sup>2,5</sup>, Sergey N. Yurchenko<sup>2</sup> , and Giovanna Tinetti<sup>2</sup>

<sup>1</sup>LATMOS/IPSL, UVSQ, Université Paris-Saclay, UPMC Univ. Paris 06, CNRS, Guyancourt, France; [jeremy.bourgalais@latmos.ipsl.fr](mailto:jeremy.bourgalais@latmos.ipsl.fr)

<sup>2</sup>Department of Physics & Astronomy, University College London, Gower Street, WC1E 6BT London, UK

<sup>3</sup>Laboratoire Interuniversitaire des Systèmes Atmosphériques (LISA), UMR CNRS 7583, Université Paris-Est-Créteil, Université de Paris, Institut Pierre Simon Laplace, Créteil, France

<sup>4</sup>Laboratoire de Chimie Physique, CNRS, Univ. Paris-Sud, Université Paris Saclay, 91405, Orsay, France

<sup>5</sup>SRON Netherlands Institute for Space Research, Sorbonnelaan 2, 3584 CA, Utrecht, Netherlands

Received 2020 February 11; revised 2020 April 7; accepted 2020 April 15; published 2020 May 28

## Abstract

With the upcoming launch of space telescopes dedicated to the study of exoplanets, the Atmospheric Remote-Sensing Infrared Exoplanet Large-survey (ARIEL) and the James Webb Space Telescope (JWST), a new era is opening in exoplanetary atmospheric explorations. However, especially in relatively cold planets around later-type stars, photochemical hazes and clouds may mask the composition of the lower part of the atmosphere, making it difficult to detect any chemical species in the troposphere or understand whether there is a surface or not. This issue is particularly exacerbated if the goal is to study the habitability of said exoplanets and search for biosignatures. This work combines innovative laboratory experiments, chemical modeling, and simulated observations at ARIEL and JWST resolutions. We focus on the signatures of molecular ions that can be found in upper atmospheres above cloud decks. Our results suggest that  $\text{H}_3^+$  along with  $\text{H}_3\text{O}^+$  could be detected in the observational spectra of sub-Neptunes based on a realistic mixing ratio assumption. This new parametric set may help to distinguish super-Earths with a thin atmosphere from  $\text{H}_2$ -dominated sub-Neptunes to address the critical question of whether a low-gravity planet around a low-mass active star is able to retain its volatile components. These ions may also constitute potential tracers to certain molecules of interest, such as  $\text{H}_2\text{O}$  or  $\text{O}_2$ , to probe the habitability of exoplanets. Their detection will be an enthralling challenge for the future JWST and ARIEL telescopes.

*Unified Astronomy Thesaurus concepts:* [Exoplanet atmospheres \(487\)](#); [Photoionization \(2060\)](#); [Space telescopes \(1547\)](#); [Laboratory astrophysics \(2004\)](#)

## 1. Introduction

Thanks to the Kepler mission (Borucki 2016), many exoplanets of a new kind, bigger than the Earth but smaller than Neptune ( $1 R_{\oplus} < R_p < 4 R_{\oplus}$ ), have been observed and constitute the majority of the worlds detected outside the solar system (Coughlin et al. 2016). Based on observations and theoretical considerations, many of these low-gravity planets seem to have thick atmospheres that retain light species ( $\text{H}_2$ , He; Jontof-Hutter 2019). However, these small planets show a great diversity of densities, suggesting a diverse range of bulk and atmospheric compositions including rocky planets with thin atmospheres mainly made of heavy molecules such as  $\text{N}_2$ ,  $\text{CO}$ , or  $\text{H}_2\text{O}$  (Elkins-Tanton & Seager 2008; Schaefer et al. 2012; Moses et al. 2013; Hu & Seager 2014; Rimmer & Rugheimer 2019).

These atmospheric constituents have a significant impact on the evolution of the planet, including its potential habitability. Many low-gravity planets are detected mainly in orbit around low-mass M-type stars, which are the most abundant stars in our galaxy (Chabrier 2003; Laughlin et al. 2004). These stars emit strongly in the ultraviolet (UV), and the atmospheric properties, as well as the dynamics and fate of their associated exoplanets, are thus strongly impacted by stellar radiation (Shkolnik & Barman 2014). Based on our current knowledge of the solar system's bodies, such as Titan (Hörst 2017), high-energy radiation, in particular in the extreme UV (EUV) range (10–120 nm), has a strong effect on the chemical composition of the atmosphere (Chadney et al. 2015). Similar effects are

therefore also expected in the atmospheres of exoplanets, especially those orbiting M dwarfs, that remain active in the EUV much longer than Sun-like G stars (luminosity factors of 10–100 times higher than the solar flux; Ribas et al. 2016; Lammer et al. 2011). The EUV radiation significantly alters the chemical composition of the upper atmosphere of exoplanets during the early phase of their evolution through interaction with the most abundant molecular species, but its long-term effect on the habitability of planets is complex and remains an open question (Wordsworth & Pierrehumbert 2014; Luger & Barnes 2015; Bolmont et al. 2016; Owen & Mohanty 2016). The thermosphere is a complex chemical environment where the main atmospheric components are dissociated and ionized, leading to efficient ion–molecule reactions involving their primary volatile elements (Moses et al. 2011). Many atmospheric chemical models, adapted mostly to hot exoplanets, are available in the literature, some of which consider the effects of metals and simple ions, like  $\text{H}_3^+$ , in nonequilibrium models (Yelle 2004; Muñoz 2007; Koskinen et al. 2013; Lavvas et al. 2014; Drummond et al. 2016; Rimmer & Helling 2016; Helling & Rimmer 2019). However, there is no existing study focused on the characterization of the main positive ions that may form within the thermosphere of warm exoplanets, and their expected important effects on the chemistry are yet to be quantified. In particular, any effect on the distribution of the IR-radiating species that drive thermal and nonthermal atmospheric escape processes will influence the retention of planetary atmospheres. Determining whether a low-gravity

planet around a small active star is able to retain its volatile components is a critical question to understand its nature and evolution. For rocky temperate planets, in particular, this question is pivotal to understand their potential habitability (Luger & Barnes 2015; Bourrier et al. 2017), since UV irradiation may also stimulate the synthesis of prebiotic molecules (Rimmer et al. 2018).

We are at the dawn of a new era in space exploration with the upcoming launch of new telescopes like the Atmospheric Remote-Sensing Infrared Exoplanet Large-survey (ARIEL; Tinetti et al. 2018) and the James Webb Space Telescope (JWST; Gardner et al. 2006). They will provide a unique insight into the thermal structure and chemical composition of the atmospheres of exoplanets due to their spectral range and array of instruments that will be used for transmission, emission, and phase-curve spectroscopy. To make the most of these future observations, it is important to learn as much as possible about their atmospheric chemistry. Among the different approaches, experimental laboratory simulation is a powerful tool for understanding the chemical evolution of an exoplanet atmosphere and also for guiding observations and the development of atmospheric models. However, so far in the literature, previous laboratory experiments have focused on solid particles (production rates, size, chemical composition) that may constitute photochemical hazes within the cold and warm atmospheres of exoplanets (He et al. 2018a, 2018b; Hörst et al. 2018; Wolters et al. 2019; Moran et al. 2020).

In order to complete this crucial phase of experimental simulation, it is also necessary to study the chemical evolution of the gas phase in the primary upper atmosphere of exoplanets following UV irradiation of host stars and to identify the abundant species that may form. While He et al. (2019) studied the neutral species involved in the gas-phase chemistry of simulated exoplanet atmospheres, the implication of the positive ions has never been studied. Photoproducts drive the formation of hazes lower in the atmosphere but are also the starting point for the formation of prebiotic molecules. To be able to detect biosignatures that will be critical to the search for life, this work creates the first milestones with innovative photochemical-driven molecular growth laboratory experiments and shows the direct relationship with space observations.

The approach in this paper aims at providing information on chemical species, in particular, charged species that are expected in the thermosphere of rocky and gas-rich exoplanets and could be detectable with future ARIEL and JWST observations. To achieve this goal and show how the combination of laboratory simulation and numerical modeling constrains the inputs in the modeling of the observations, this work has been divided into three steps.

In the first step, we experimentally simulated the effect of UV radiation on simplified gas-phase samples ( $\text{H}_2\text{-CO-N}_2\text{-H}_2\text{O}$ ) whose variation of the hydrogen mixing ratio allows us to mimic cases of super-Earths and mini-Neptunes. This first experimental study allowed the measurements of both neutral and cations and identification of the main positive ions formed in  $\text{H}_2$ -poor and  $\text{H}_2$ -rich environments.

In the second step, we analyzed the main pathways of formation of these ions using a photochemical model. The characterization of the photoproducts and the identification of key reactions allowed us to confirm that these experimental results were transposable to planetary environments and that

these species could also be formed in significant abundance in the thermospheres of exoplanets.

In the third step, we carried out simulations of observations using the resolution of the future JWST and ARIEL instruments to determine whether it was possible to detect in a transmission spectrum of an exoplanet two of the major ions observed in laboratory experiments with realistic mixing ratios. Due to the lack of chemical information on the atmospheres of exoplanets, we chose a planet whose composition most closely resembles one of the gaseous mixtures used in the laboratory (mini-Neptune GJ1214b), where CO replaced by methane is the only difference, but whose impact on the formation of ions is nil.

## 2. Methods

### 2.1. Photochemical Reactor Coupled to an EUV Photon Source

Simplified super-Earth and mini-Neptune atmospheres are reproduced in the laboratory using a photochemical reactor that has already been used in the past for photochemical experiments simulating complex environments similar to the upper layers of planetary atmospheres (Carrasco et al. 2013; Peng et al. 2014; Bourgalais et al. 2019). The cell is filled with a gas mixture representative of the environments to be reproduced. The species of the gas mixture are then irradiated by an EUV photon source, which is directly coupled to the photochemical reactor. The energetic particles are produced by a microwave plasma discharge of a rare gas at low pressure providing radiation at different wavelengths depending on the gas used (Tigrine et al. 2016). The chemical species present in the reactor are probed at a steady state using a quadrupole mass spectrometer (Hiden Analytical EQP 200 QMS) to measure neutral compounds and positive ions with a high sensitivity below the parts-per-million (ppm) level (Bourgalais et al. 2019; Dubois et al. 2019).

In this work, we use a surfatron-type discharge with a neon gas flow that allows us to irradiate the gas mixture of the photochemical cell at an overall pressure of 0.9 mbar and at room temperature. The pressure is adjusted to represent the atmospheric pressures of exoplanets but is experimentally constrained in the simulated environments. Reaching the low pressures found in the higher layer of exoplanet environments is not possible due to experimental constraints. The configuration of the device shown in Bourgalais et al. (2019) shows that the inlet of the mass spectrometer (MS) is located very close to the outlet of the vacuum UV lamp in order to limit wall effects, and as a consequence, the working pressure is adjusted to ensure that reactions will take place before detection with the MS. The working pressure is barely higher than the pressure (ca. 0.01–0.1 mbar) at which EUV radiation penetrates (Lavvas et al. 2014) and low enough to avoid termolecular effects as in the actual low-density exoplanet thermospheres. Thus, the higher pressure increases the kinetics in the experiments, but the results obtained on the chemistry of the ions remain transposable to the atmospheres of exoplanets. The temperatures of the thermospheres of exoplanets can reach tens of thousands of Kelvin, whereas our experiments were conducted at room temperature. However, in the lower part of the thermospheres, the deposition of stellar energy can be compensated mainly by the radiative emission of cooling ions and the subsequent ion chemistry, so that the temperature can drop to 1000 or even a few hundred K (Yelle 2004; Koskinen

et al. 2007). At these relatively high temperatures, the temperature dependence of the rate coefficients and branching ratios (BRs) can be very important. Therefore, it should be noted that the temperature dependence of the formation pathways of the main ions highlighted in this work was studied with a one-cell (OD) photochemical model described in the following section. Numerical simulations performed at room temperature and 1000 K show the same major ions for the two extreme cases discussed in this article. As a conclusion, the simulated environments are relevant to study photochemical mechanisms in the upper layers of cold and potentially warm exoplanetary atmospheres (<1000 K), but these extrapolations at high temperatures must be taken with caution, as there are few data on rate coefficients and BRs in the literature.

A wavelength of 73.6 nm corresponding to a photon energy of 16.8 eV is used with a flux of about  $10^{14}$  photons  $\text{cm}^{-2} \text{s}^{-1}$  leading to an ionization rate of ca.  $10^{-6}$ . This wavelength is chosen to reach the ionization threshold of the chemical species of the gas mixture that is composed of  $\text{H}_2$ , CO, and  $\text{N}_2$ . With this wavelength and the pressure in the reactor, we mimic the stellar EUV field of a star in an upper atmospheric layer (France et al. 2016; Loyd et al. 2016; Youngblood et al. 2016). Transitional planets with a size between Earth and Neptune appear to have a diversity of compositions that is not well explained; however, everyone agrees that low-density planets are mainly composed of molecular hydrogen, but some super-Earths and mini-Neptunes will likely have thick atmospheres that are not  $\text{H}_2$ -dominated. Bulk atmospheric composition could have a wide variety of elemental abundance ratios in which the amount of  $\text{H}_2$  has profound effects on the evolution of the atmosphere (Pierrehumbert & Gaidos 2011). Our approach is to use gas mixtures containing  $\text{H}_2$  along with other expected important molecules in upper layers of cool super-Earth atmospheres. We vary only the relative proportions of  $\text{H}_2$  within a large range to test the contribution of  $\text{H}_2$  to the formation of photoproducts in the cases of  $\text{H}_2$ -poor and  $\text{H}_2$ -rich environments that are representative of simplified super-Earth and mini-Neptune upper atmospheres (Rimmer & Rugheimer 2019). We focus on Earth-like planets by adding  $\text{N}_2$  to the gas mixtures (Wordsworth & Pierrehumbert 2014) containing  $\text{H}_2$ , and since the bulk atmospheric composition of such an environment is defined and affected largely in terms of the C/O ratio, CO is added as the only major source of carbon and oxygen to keep a ratio of 1 (Rimmer & Rugheimer 2019). Three gas mixtures have been used with different initial fractional abundances of  $\text{H}_2$ . The first is a gas mixture at 1%  $\text{H}_2$ , the second is an intermediate at 33%  $\text{H}_2$ , and the third is a mixture at 96%  $\text{H}_2$ . The mixing ratio of  $\text{N}_2$  was arbitrarily chosen to be equal to that of CO. Finally, water vapor is the major trace species at the ppm level in the reactor coming from residual adsorption on the reactor walls. Contrary to a previous study on Titan conducted with the same device in Bourgalais et al. (2019), here the reactor was not heated to minimize the presence of residual water, and the pressure in the reactor is higher (0.9 mbar in this work versus 0.01 mbar in Bourgalais et al. 2019). Gao et al. (2015) showed that water vapor can have profound effects on the evolution of the planet's atmosphere. Thus, the presence of water vapor traces in the reactor provides a study of the impact of trace levels of water vapor in the atmosphere of exoplanets.

Mass spectra reported in this study are the average of 10 scans obtained at  $2 \text{ s amu}^{-1}$  with a channeltron-type detection

over the 1–50 amu mass range. In all spectra presented below, signals with intensities lower than 1000 cps are considered as background noise. The reported mass spectra show the direct signal recorded without background subtraction. The duration of the irradiation is only a few minutes because, as the numerical simulations in this manuscript show, the state of equilibrium is reached in less than 1 ms for the main species because their abundance is constant. The stability of the ion signal over the 10 mass spectra recorded during the irradiation supports the claim that the steady state is reached very quickly.

## 2.2. 0D Photochemical Model

To interpret the experimental mass spectra, a coupled ion-neutral photochemical model was used to reproduce the chemistry occurring in the reactor. The model has been detailed in the literature (Peng et al. 2014). Here we provide a short description, mentioning the main updates since the initial paper.

### 2.2.1. The Reactor Model

We consider a simplified 0D geometry of the reactor, assuming a uniform spatial distribution of the species. The gas inflow and outflow are taken into account to ensure a constant pressure, and radiative transfer is treated through Beer–Lambert-type photoabsorption, in the assumption of a uniform gas. The chemical reactions are treated as a system of ordinary differential equations (ODEs).

The implicit–explicit Runge–Kutta–Chebyshev (IRKC) method (Shampine et al. 2006) is used to integrate the system of partial differential equations. The photolysis and transport are treated explicitly (complex evaluation of Jacobian elements for radiative transfer makes it impractical to regard the photolysis rate equations as ODEs). The chemical ODEs are treated implicitly. The IRKC method handles stiff ODE systems (Verwer & Sommeijer 2004).

The Fortran Reactor code is publicly available at <https://github.com/ppernot/Reactor>, with bash scripts for execution of parallel Monte Carlo runs on an OpenStack cloud (CloudReactor<sup>6</sup>). A graphical interface (ReactorUI<sup>7</sup>) is provided for the analysis of the results.

### 2.2.2. Chemistry

*The MC-ChemDB Database.* The MC-ChemDB database (MC-ChemDB<sup>8</sup>) has been designed to handle the uncertainty on the rate parameters of chemical reactions (Hébrard et al. 2006, 2009; Carrasco et al. 2008; Plessis et al. 2012) and photolysis processes (Gans et al. 2010; Peng et al. 2014). The principle is based on a server–client architecture. The server generates and hosts random sets of databases for Monte Carlo uncertainty propagation (BIPM et al. 2008). The client gathers the required number of samples for adapted chemical schemes: depending on the gas mixture in the reactor, only the pertinent subset of the database is used.

The database is split into three modules (neutral reactions, ionic reactions, and photolysis) that require different treatments to generate random reaction rate parameters.

<sup>6</sup> <https://github.com/ppernot/CloudReactor>

<sup>7</sup> <https://github.com/ppernot/ReactorUI>

<sup>8</sup> <https://github.com/ppernot/MC-ChemDB>

Neutral chemistry (bimolecular thermal reactions and termolecular thermal recombinations) is built from Hébrard et al. (2006, 2009) and Dobrijevic et al. (2016). Bimolecular rate constants are represented with the Kooij (modified Arrhenius) rate law and termolecular association with a pressure-dependent Lindeman–Trope rate law (Dobrijevic et al. 2016; Vuitton et al. 2019). The scheme is based on partial rate constants.

Ionic chemistry (ion–molecule reactions and dissociative recombinations) is built from Carrasco et al. (2008) and Plessis et al. (2012). Rate laws for ion–neutral reactions are mostly based on the Langevin law, with temperature-dependent laws of the type ionpol (Wakelam et al. 2012) for molecules with nonzero dipole moments. Dissociative recombinations are based on a modified Arrhenius rate law (Plessis et al. 2012). The global reaction rates and BRs are treated separately.

Photoprocesses (photodissociation and photoionization), cross sections, and BRs are extracted from the Leiden database (<https://home.strw.leidenuniv.nl/~ewine/photo/>; Heays et al. 2017). If BRs are not provided by Leiden, they are extracted from SWRI (<https://phidrates.space.swri.edu>; Huebner & Mukherjee 2015), except for CH<sub>4</sub>, where the representation by Peng et al. (2014) is used. Cross sections are provided with 1 and 0.1 nm resolutions. At this stage, the temperature dependence of the cross sections and BRs is ignored.

For a description of the parameter uncertainty representations, see Peng et al. (2014). The database was originally oriented on the chemistry of H-, C-, and N-bearing species, and it has recently been upgraded to account for oxygenated species from Vuitton et al. (2019) and the KIDA database (Wakelam et al. 2012).

*The photochemical scheme.* According to the following procedure, a consistent set of reactions is iteratively generated from the irradiated initial mixture (H<sub>2</sub>/N<sub>2</sub>/CO/H<sub>2</sub>O):

1. select all reactions involving the list of species;
2. update the list of species with the generated products; and
3. iterate to (1) until no new species is produced.

The resulting chemical model contains 54 photoprocesses (photolysis of N<sub>2</sub>, H<sub>2</sub>, CH<sub>4</sub>, C<sub>2</sub>H<sub>2</sub>, C<sub>2</sub>H<sub>4</sub>, C<sub>2</sub>H<sub>6</sub>, HCN, NH<sub>3</sub>, CO, and H<sub>2</sub>O), 903 neutral reactions (811 bimolecular and 92 termolecular), and 1941 ion processes (1314 bimolecular and 687 dissociative recombinations). The chemical model involves 177 neutral species, 190 positive ions with masses up to 130, and electrons.

*Simulations.* The model simulates chemistry under conditions similar to those of the experiments (Bourgalais et al. 2019). It is run for a long enough time to reach a stationary state (1 s), and the stationary mole fractions of the products are compared with the experimental data. Complementary Monte Carlo simulations are performed to evaluate the uncertainty on the model predictions (500 runs). A global rate analysis is performed to identify key reactions and dominant formation pathways (Hébrard et al. 2009).

### 2.3. Simulations of Observations with ARIEL and JWST

We investigate the feasibility of detecting the ions H<sub>3</sub><sup>+</sup> and H<sub>3</sub>O<sup>+</sup> in sub-Neptune-type planets using the radiative transfer code TauREx3 (Waldmann et al. 2015a, 2015b). Our approach consists of simulating a high-resolution spectrum using TauREx in forward mode. Then we use our instrument simulators, ArielRad (Mugnai et al. 2019), to bin down the

**Table 1**  
List of IR Opacities Used in This Work

Species	References
H <sub>2</sub> –H <sub>2</sub>	Abel et al. 2011; Fletcher et al. 2018
H <sub>2</sub> –He	Abel et al. 2012
H <sub>2</sub> O	Barton et al. 2017; Polyansky et al. 2018
CH <sub>4</sub>	Hill et al. 2013; Yurchenko et al. 2014
H <sub>3</sub> <sup>+</sup>	Mizus et al. 2017
H <sub>3</sub> O <sup>+</sup>	Yurchenko et al. 2020

observations and estimate the instrument noise. As we are investigating the theoretical detection biases through retrieval techniques, we do not scatter the observed spectra (Feng et al. 2018; Changeat et al. 2019). Finally, we retrieve the simulated observations using TauREx3 to check whether the ion signals can be statistically recovered.

We base our simulations on the bulk parameters for GJ1214b from Harpsøe et al. (2013): we use a planet radius of 0.254 R<sub>J</sub>, a planet mass of 0.0197 M<sub>J</sub>, and a star radius of 0.216 R<sub>S</sub>. In the case of ARIEL, we consider that all of the Tier 3 observations for this planet are stacked together (total of 10 transits; Tinetti et al. 2016), while for JWST, we combine single observations from NIRISS and NIRSpec (total of two transits) to roughly match the wavelength coverage. The atmosphere is assumed to be isothermal at 700 K and filled with H<sub>2</sub> and He. We add the trace gases H<sub>2</sub>O and CH<sub>4</sub> along with the two ions H<sub>3</sub><sup>+</sup> and H<sub>3</sub>O<sup>+</sup>. For our simplified model, the abundances for H<sub>2</sub>O and CH<sub>4</sub> are set to 10<sup>−5</sup> and are constant with altitude. For the ions, we base our input abundances on profiles resembling those from Helling & Rimmer (2019). As is expected for sub-Neptune-type planets, we enhance their abundance findings by approximately 1 order of magnitude and use the two-layer model (Changeat et al. 2019) to describe the abundance decrease deeper in the atmosphere. For H<sub>3</sub><sup>+</sup>, the top abundance is 10<sup>−5</sup> and the surface abundance is 10<sup>−14</sup> with a layer pressure change at 10<sup>−5</sup> bar. For H<sub>3</sub>O<sup>+</sup>, the top abundance is also 10<sup>−5</sup> and the surface abundance is 10<sup>−14</sup>. The layer change is done deeper at 10<sup>−3</sup> bars. On top of this, we add a gray cloud cover that is fully opaque below 5 × 10<sup>−3</sup> bars, as expected for this planet (Kempton et al. 2011; Morley et al. 2013; Kreidberg et al. 2014). For the molecular absorptions, we use the most up-to-date molecular line lists from the ExoMol project (Tennyson et al. 2016), HITEMP (Rothman et al. 2010), and HITRAN (Gordon et al. 2016) and build the cross-section tables at a resolution of 10,000. We also consider absorptions from Rayleigh scattering and collision-induced absorption (only the pairs H<sub>2</sub>–H<sub>2</sub> and H<sub>2</sub>–He). The list of opacities used in this paper is summarized in Table 1.

For our retrieval step, the parameter space is explored using the Multinest algorithm (Feroz et al. 2009) with 500 live points and an evidence tolerance of 0.5. The list of retrieved parameters and their corresponding uniform prior bounds is shown in Table 2.

## 3. Results

### 3.1. Identification by Mass Spectrometry of the Neutral Species Formed in the Experiments

A typical measured neutral mass spectrum is shown in Figure 1 and displays the abundant peaks of the initial gas mixture species H<sub>2</sub> (m/z = 2), CO, and N<sub>2</sub> (both at m/z = 28,

**Table 2**

List of Retrieved Parameters and Their Corresponding Uniform Prior Bounds

Parameter	Mode	Bounds
Radius	Linear	0.1–0.4 $R_j$
H <sub>2</sub> O	Log	0.1–10 <sup>-12</sup>
CH <sub>4</sub>	Log	0.1–10 <sup>-12</sup>
H <sub>3</sub> <sup>+</sup>	Log	0.1–10 <sup>-12</sup>
H <sub>3</sub> O <sup>+</sup>	Log	0.1–10 <sup>-12</sup>
Temperature	Linear	300–1500 K
Cloud pressure	Log	10–10 <sup>-7</sup> bars

with isotopologues at  $m/z$  of 29, 30, and 31). Atomic species H, C, N, and O resulting from the fragmentation of their parental molecules upon photodissociation are observed at  $m/z$  of 1, 12, 14, and 16, respectively. Peaks at  $m/z$  of 20, 21, and 22 match the isotope relative abundances of neon, which is the nonreactive gas flowing continuously in the photochemical reactor. A peak at  $m/z$  of 10 is attributed to double ionized <sup>20</sup>Ne<sup>2+</sup>, produced in the MS itself by electron impact ionization at 70 eV for the detection of neutral species. Finally, we also observed peaks at  $m/z$  of 17 (OH) and 18 (H<sub>2</sub>O).

We are conducting our experiments in an open system, where the gas mixture is introduced and pumped continuously. In the reactor, the residence time is short, making it difficult to detect neutral molecules larger than 40 amu. Neutral species beside the initial gas mixture contain only atomic species H, C, N, and O resulting from the fragmentation of their parental molecules upon photodissociation; neon, which is a nonreactive gas flowing continuously in the photochemical reactor; and small molecules formed during the first reaction such as CO<sub>2</sub>.

Thus, the experimental results obtained for neutral species in this work do not provide as much information, and the rest of the study will focus on positive ions, about which our knowledge in this type of environment is much more limited. It should also be noted that the rate of production of ionic products relative to neutral products is similar, with molar

fractions of the order of ppm relative to neutral species in the initial gas mixtures.

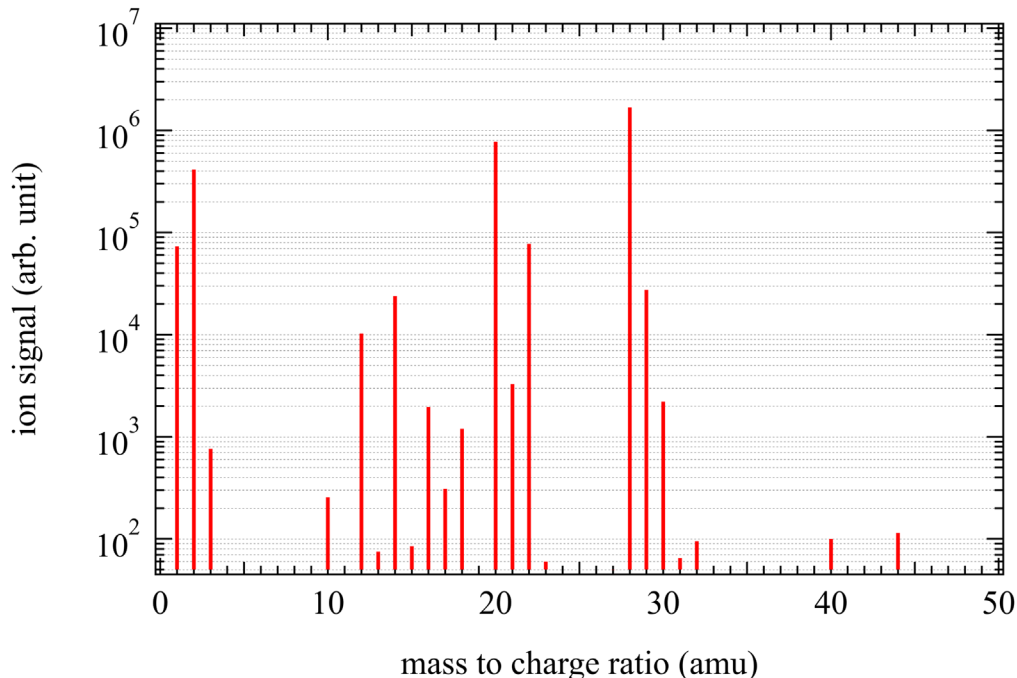
### 3.2. Identification by Mass Spectrometry of the Main Ions Formed in the Experiments

Figure 2 shows in situ nonnormalized gas-phase mass spectra of cationic species at their stationary point in the reactor after 15 minutes of EUV irradiation at an overall pressure of 0.9 mbar. The species are detected at  $m/z$  1, 2, 3, 18, 19, 20, 21, 28, 29, 30, 31, and 32 above the limit of the background noise;  $m/z$  1, 2, and 3 are attributed to H<sup>+</sup>, H<sub>2</sub><sup>+</sup>, and H<sub>3</sub><sup>+</sup>, respectively. Due to the high sensitivity of the MS, H<sub>2</sub>O<sup>+</sup> and its protonated form H<sub>3</sub>O<sup>+</sup> are detected along with the first H<sub>3</sub>O<sup>+</sup> isotopologues (molecules that only differ in their isotopic composition) at  $m/z$  18, 19, 20, and 21. Finally,  $m/z$  28, 29, 30, 31, and 32 are attributed to N<sub>2</sub><sup>+</sup> and CO<sup>+</sup>, HCO<sup>+</sup>, and/or N<sub>2</sub>H<sup>+</sup> along with the first HCO<sup>+</sup> isotopologues. The first notable result is that the most abundant ions at  $m/z$  19 and 29 remain the same with all gas mixtures. The formation of H<sup>+</sup>, H<sub>2</sub><sup>+</sup>, and H<sub>3</sub><sup>+</sup> ions (named H<sub>x</sub> ions) does not follow the same trend as the primary ions N<sub>2</sub><sup>+</sup> and CO<sup>+</sup> at mass 28, which are formed by the ionization of N<sub>2</sub> and CO. In the case of H<sub>2</sub>-rich gas mixtures, H<sub>x</sub> ions and, in particular, H<sub>3</sub>O<sup>+</sup> dominate, while the primary ions N<sub>2</sub><sup>+</sup> and CO<sup>+</sup> occur in significant amounts in the case of gas mixtures where H<sub>2</sub> is not in the majority.

### 3.3. Unraveling the Chemical Processes through Ion-neutral Modeling

#### 3.3.1. Hydrogen-poor Atmospheres

Figure 3 displays the simulated evolution of the mole fractions of the main ionic photoproducts after irradiation at 73.6 nm of the H<sub>2</sub>/CO/N<sub>2</sub> gas mixture with an H<sub>2</sub> mixing ratio of 1%. The two most abundant predicted ions using the 0D photochemical model are HCO<sup>+</sup> and H<sub>3</sub>O<sup>+</sup>, as observed in the experimental mass spectrum of Figure 2. The main HCO<sup>+</sup> formation pathways are found to be through the reactions R1,



**Figure 1.** Typical in situ gas-phase mass spectrum of neutral species present in the reactor with an H<sub>2</sub>-CO-N<sub>2</sub> gas mixture after EUV irradiation.

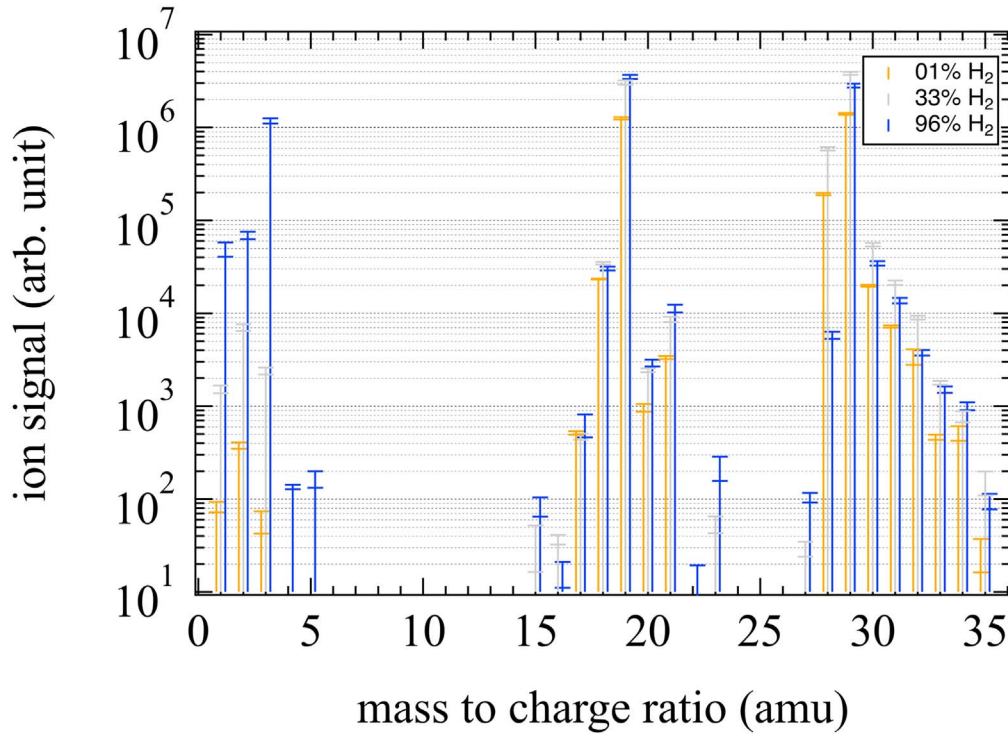
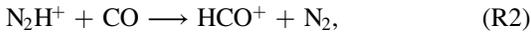
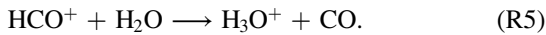


**Figure 2.** Positive ions measured after irradiation at 73.6 nm of  $\text{H}_2/\text{CO}/\text{N}_2$  gas mixtures. The  $\text{H}_2$  mixing ratios were chosen at 1% (orange), 33% (gray), and 96% (blue) at an overall pressure in the reactor of 0.9 mbar. Twice the standard deviation,  $2\sigma$ , in 10 measurements of each mass is displayed.

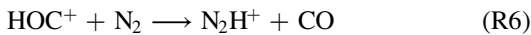
R2, and R3. Though  $\text{HOC}^+$  is formed in a second exit channel of R1, it is rapidly converted into  $\text{HCO}^+$  through proton transfer (R3):



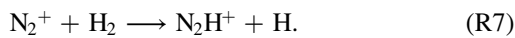
The main loss pathways of  $\text{HCO}^+$  are found to be dissociative recombination with electrons, along with the proton transfer reaction with water (R4 and R5):



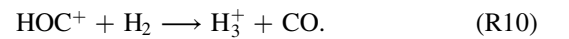
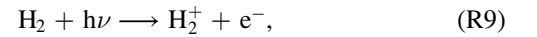
Using trace water vapor in the reactor, R5 is the dominant formation pathway for  $\text{H}_3\text{O}^+$ . The  $\text{H}_3\text{O}^+$  is consumed through dissociative recombination leading to water and OH radicals. Modeling of the chemistry within the reactor also shows that the formation of  $\text{N}_2\text{H}^+$  is negligible compared to that of  $\text{HCO}^+$ . Its main production pathways are



and



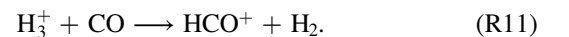
The low abundance of  $\text{N}_2\text{H}^+$  compared to  $\text{HCO}^+$  is due to the efficient reaction R2, showing the propensity of CO to consume  $\text{N}_2\text{H}^+$  to produce  $\text{HCO}^+$ . As observed in the experimental mass spectrum, the  $\text{H}_x$  ions are expected to be negligible through the main reactions (R8, R9, and R10):



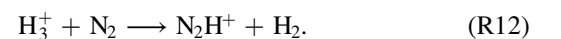
Indeed,  $\text{HOC}^+$  mainly reacts with  $\text{N}_2$  and CO (R3 and R6) to produce  $\text{N}_2\text{H}^+$  and  $\text{HCO}^+$ , respectively, rather than with  $\text{H}_2$ .

### 3.3.2. Hydrogen-rich Atmospheres

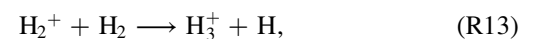
Figure 4 displays the simulated evolution of the mole fractions of the main ionic photoproducts after irradiation at 73.6 nm of the  $\text{H}_2/\text{CO}/\text{N}_2$  gas mixture with an  $\text{H}_2$  mixing ratio of 96%. The two most abundant predicted ions using the 0D photochemical model remain  $\text{HCO}^+$  and  $\text{H}_3\text{O}^+$ , as observed in the experimental mass spectrum of Figure 2. However, the main formation pathway for  $\text{HCO}^+$  is still via R3 but with an additional parallel reaction involving  $\text{H}_3^+$ :



Independent of the mixing ratio of  $\text{H}_2$ , the main destruction pathways of  $\text{HCO}^+$  remain the same in both  $\text{H}_2$  environments (R4 and R5), which include the main production pathway for  $\text{H}_3\text{O}^+$  (R5). Compared to the case of  $\text{H}_2$ -poor atmospheres, the mole fraction of  $\text{N}_2\text{H}^+$  increases significantly in the presence of a large abundance of  $\text{H}_2$  due to a production pathway more efficient than R6 and R7:



In this  $\text{H}_2$ -rich environment,  $\text{H}_3^+$  starts to be the dominant ion due to a more efficient formation pathway,



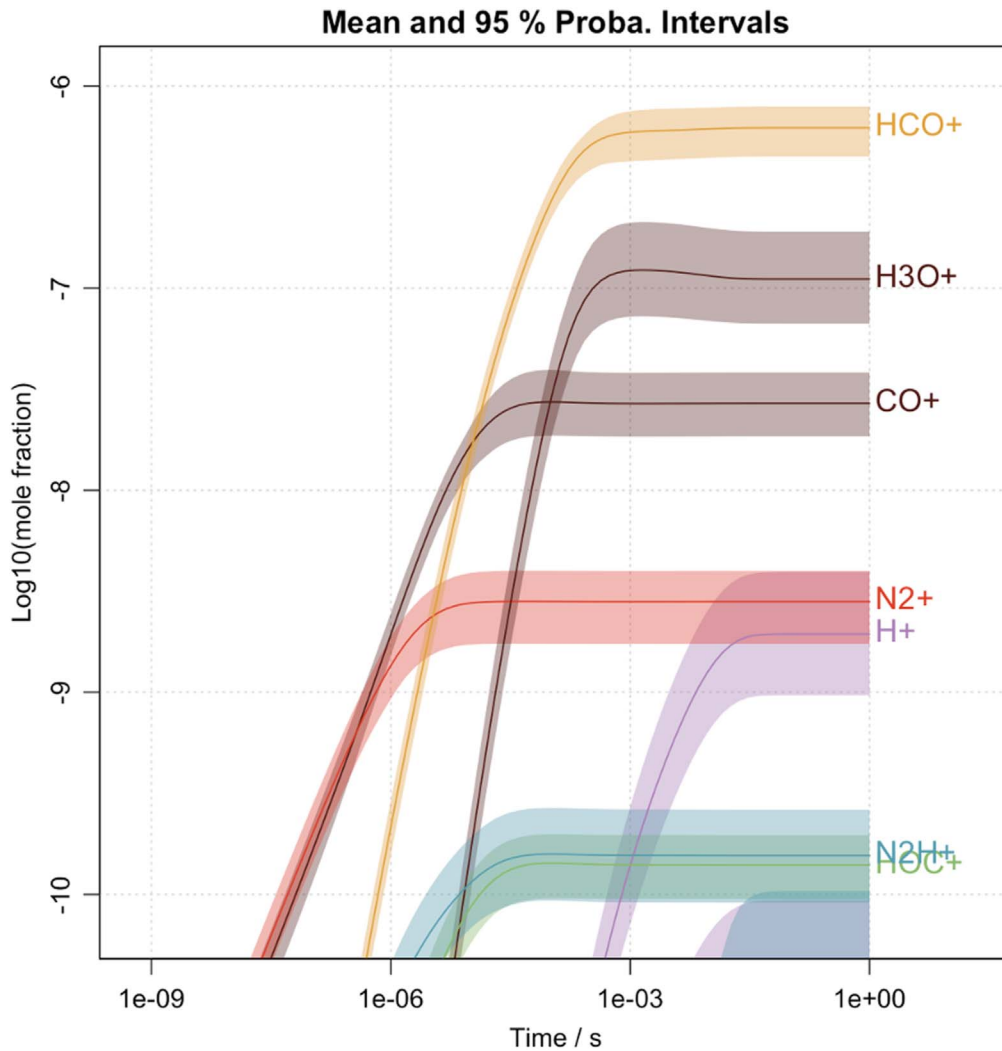


**Figure 3.** Simulated evolution of the mole fractions of the main ionic photoproducts after irradiation at 73.6 nm of the  $\text{H}_2/\text{CO}/\text{N}_2$  gas mixture with an  $\text{H}_2$  mixing ratio of 1%. All species with a mole fraction above  $10^{-11}$  are represented.

which supersedes R10. Once formed,  $\text{H}_3^+$  leads to the formation of the dominant ions  $\text{HCO}^+$  and  $\text{N}_2\text{H}^+$  by R11 and R12, respectively.

### 3.3.3. Comparison of the Two Cases

Laboratory simulations show that the same main ions ( $\text{HCO}^+$  and  $\text{H}_3\text{O}^+$ ) are observed in  $\text{H}_2$ -poor and  $\text{H}_2$ -rich environments. This implies that we can expect to observe similar contributions of these ions in the thermospheres of super-Earths and mini-Neptunes. However, they are formed through different chemical pathways by H-transfer reactions leading to the observed stable protonated ions. Another remarkable result is that even with trace amounts of water, the formation of the hydronium ion ( $\text{H}_3\text{O}^+$ ) is very effective. These results highlight the need to accurately model ion-neutral chemistry in atmospheric models of exoplanets. In the case of the low- $\text{H}_2$  environment, the primary ions  $\text{N}_2^+$  and  $\text{CO}^+$  formed at 73.6 nm trigger the molecular growth reacting with  $\text{H}_2$ . In the specific case of environments rich in  $\text{H}_2$ , the triatomic hydrogen ion  $\text{H}_3^+$  is one of the most abundant ions and is shown to be very reactive, leading to the formation of heavier ions ( $\text{N}_2\text{H}^+$  and  $\text{HCO}^+$ ).

## 3.4. Simulations of Observations with ARIEL and JWST

### 3.4.1. Choice of the Planet Type and Ion Targets

The fact that the  $\text{H}_3^+$  ion is predicted to be abundant and highly reactive leading to the formation of heavier ions in  $\text{H}_2$ -rich environments is of great interest in the context of exoplanetary observations considering the upcoming launches of the ARIEL and JWST instruments. The abundance and distribution of  $\text{H}_3^+$ , the stable ionic form of  $\text{H}_2$ , is essential to understand the chemistry and get information about the thermal structure, dynamic, and energy balance of exoplanet atmospheres (Miller et al. 2000). The  $\text{H}_3^+$  has been thoroughly studied in the mid-IR on Jupiter (Stallard et al. 2001), Saturn (Geballe et al. 1993), and Uranus (Trafton et al. 1993), but detection in the thermosphere of hot Jupiter exoplanets, with a predicted mixing ratio ranging from  $10^{-6}$  to  $10^{-4}$ , so far remains illusive (Shkolnik et al. 2006; Lenz et al. 2016). Helling & Rimmer (2019) assumed that the formation pathway of  $\text{H}_3^+$  through the ionization of  $\text{H}_2$  (R11), although very efficient, is difficult in hot exoplanet atmospheres due to the thermal decomposition of  $\text{H}_2$ , which becomes important when the temperature reaches 1000 K (Yelle 2004). Indeed, the very hot thermospheres of these exoplanets ( $>8000$  K), combined

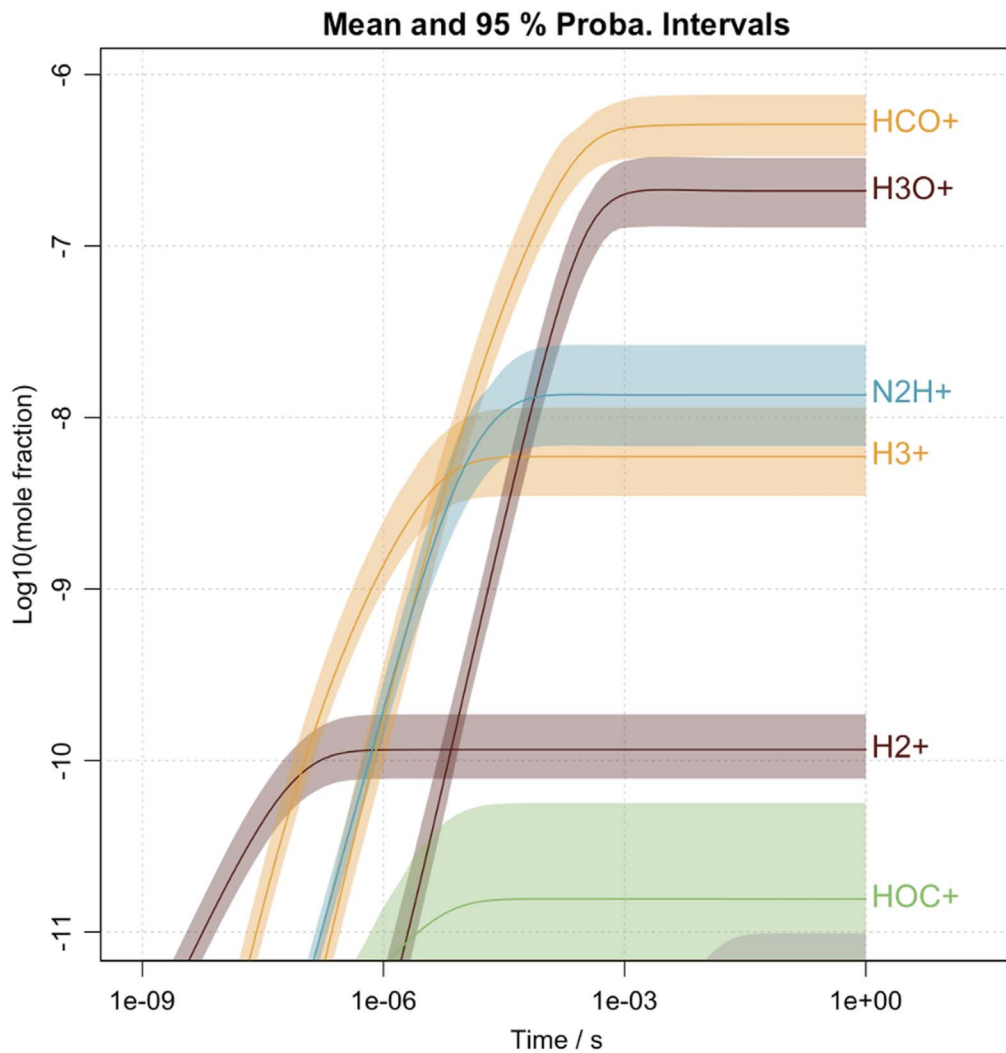


**Figure 4.** Simulated evolution of the mole fractions of the main ionic photoproducts after irradiation at 73.6 nm of the  $\text{H}_2/\text{CO}/\text{N}_2$  gas mixture with an  $\text{H}_2$  mixing ratio of 96%. All species with a mole fraction above  $10^{-11}$  are represented.

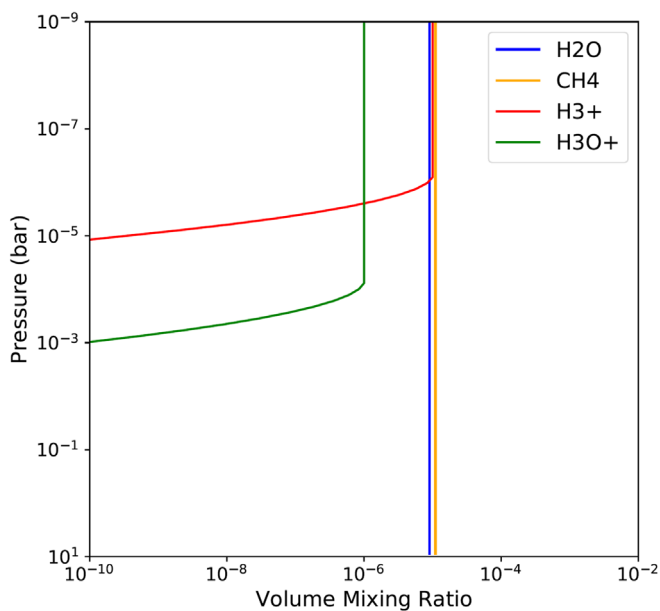


**Figure 5.** Atmospheric profiles used as input for forward simulations of an exoplanet spectrum, as well as for fitting data in retrievals.

with very intense stellar irradiations, promotes the formation of atomic neutral and  $\text{H}^+$ , making the detection of  $\text{H}_3^+$  difficult (Koskinen et al. 2010). However,  $\text{H}_3^+$  is an efficient coolant up to 10,000 K, the temperature above which thermal dissociation becomes significant, and this thermostat effect is important in controlling the atmospheric stability of giant exoplanets (Neale et al. 1996; Miller et al. 2010, 2013). By lowering the temperature of the exosphere and the related pressure,  $\text{H}_3^+$  helps to counteract the atmospheric escape of atomic and molecular species. Theory predicts that the cooling potential of  $\text{H}_3^+$  would allow one to observe  $\text{H}_3^+$  in giant exoplanets inside 0.2–1 au orbits (Yelle 2004; Koskinen et al. 2007; Miller et al. 2013). The  $\text{H}_3^+$  is able to offset the increased heating due to EUV radiation, which allows it to produce increased ion densities by photoionization. Thus, to get sufficient  $\text{H}_3^+$ , an atmosphere that is relatively cold or far enough from its star to have a low-temperature thermosphere is needed. The results of the laboratory experiments in this work suggest that colder atmospheres dominated by  $\text{H}_2$  would be more conducive to  $\text{H}_2$  stability leading to a higher  $\text{H}_3^+$  abundance. Warm Neptunes (ca. 400–800 K) would therefore potentially be better candidates than hot Jupiters for the detection of  $\text{H}_3^+$ .

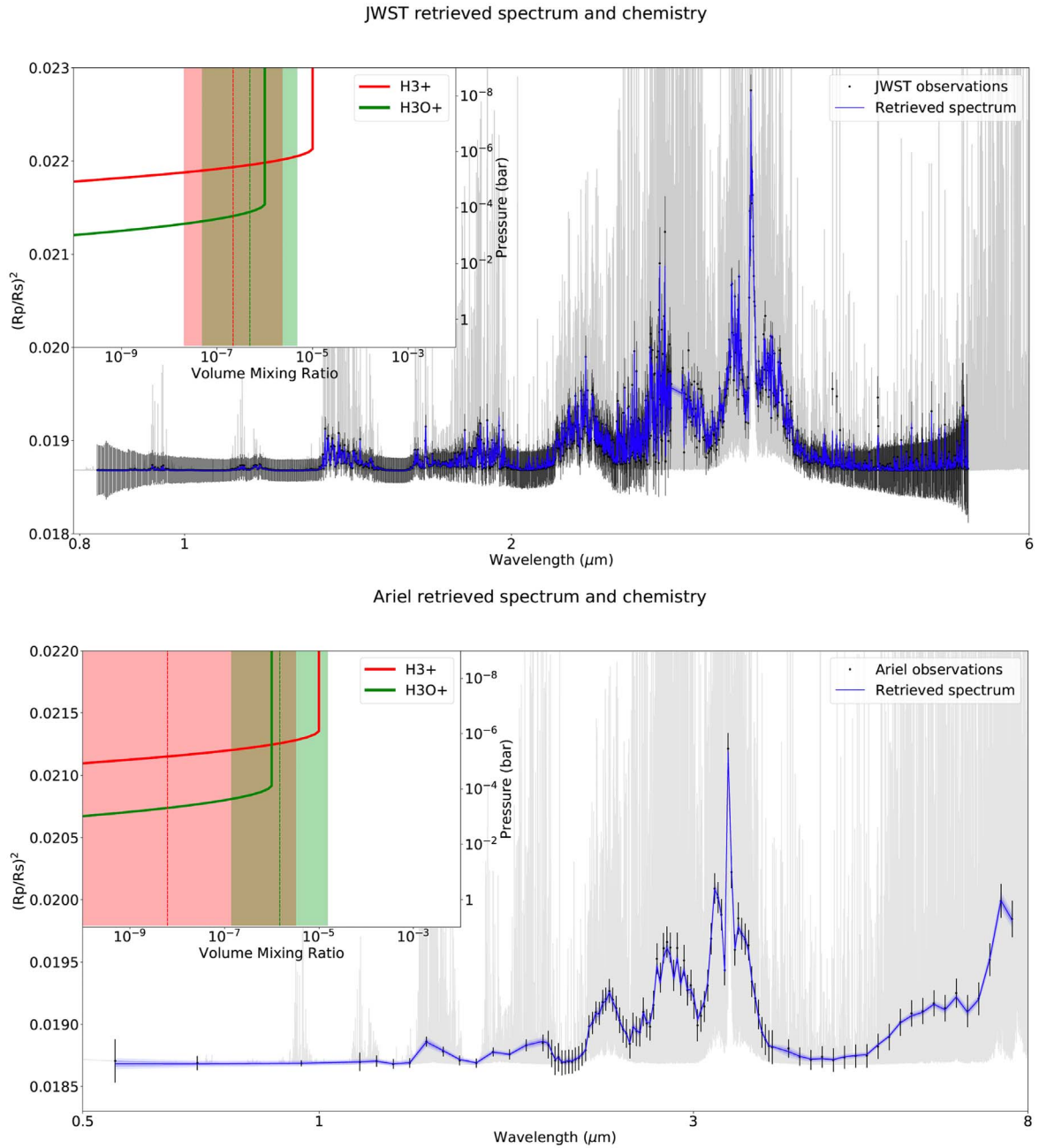


**Figure 6.** Retrieved spectra and volume mixing ratios for our JWST (top) and ARIEL (bottom) simulations of a GJ1214b-like planet with  $\text{H}_3\text{O}^+$  and  $\text{H}_3^+$  ions. For the abundances, the solid line is the true value, the dashed line is the mean retrieved value, and the shaded area represents the  $1\sigma$  retrieved value.

Like  $\text{H}_3^+$ , long lifetimes associated with certain excited states can lead to population trapping and unexpected state distributions in nonthermalized environments. A recent theoretical study by Melnikov et al. (2016) calculated the stability of the rovibrational states of  $\text{H}_3\text{O}^+$ , the lifetimes of individual states, and the overall cooling rates. In diffuse and dense regions of the interstellar medium, such as comets and molecular clouds (Goicoechea & Cernicharo 2001; Barber et al. 2009),  $\text{H}_3\text{O}^+$  is present in abundance. So far, no attempt has been made to observe  $\text{H}_3\text{O}^+$  in the thermospheres of exoplanets, although it may, like  $\text{H}_3^+$ , act as a cooling agent and bring some constraints on the physical parameters of the atmosphere.

#### 3.4.2. Simulation of the Observation of Ions in a GJ1214b-like Planet by ARIEL and JWST

In order to evaluate the ability of future telescopes to detect these two ions, we simulate a simplified atmosphere for a GJ1214b-type warm Neptune planet as observed by JWST and ARIEL with, respectively, two and 10 stacked transits. The chemical profiles we use for the  $\text{H}_3^+$  and  $\text{H}_3\text{O}^+$  ions are inspired by the work of Helling & Rimmer (2019); we also include the absorption of  $\text{H}_2\text{O}$  and  $\text{CH}_4$ , which are the main absorbers. For our simplified model, the abundances for water vapor and methane are set to 10 ppm and are constant with altitude. Those two molecules are predicted to be abundant in sub-Neptune planets (Kempton et al. 2011; Venot et al. 2014; Hu 2015; Tinetti et al. 2018; Changeat et al. 2019) and have very strong

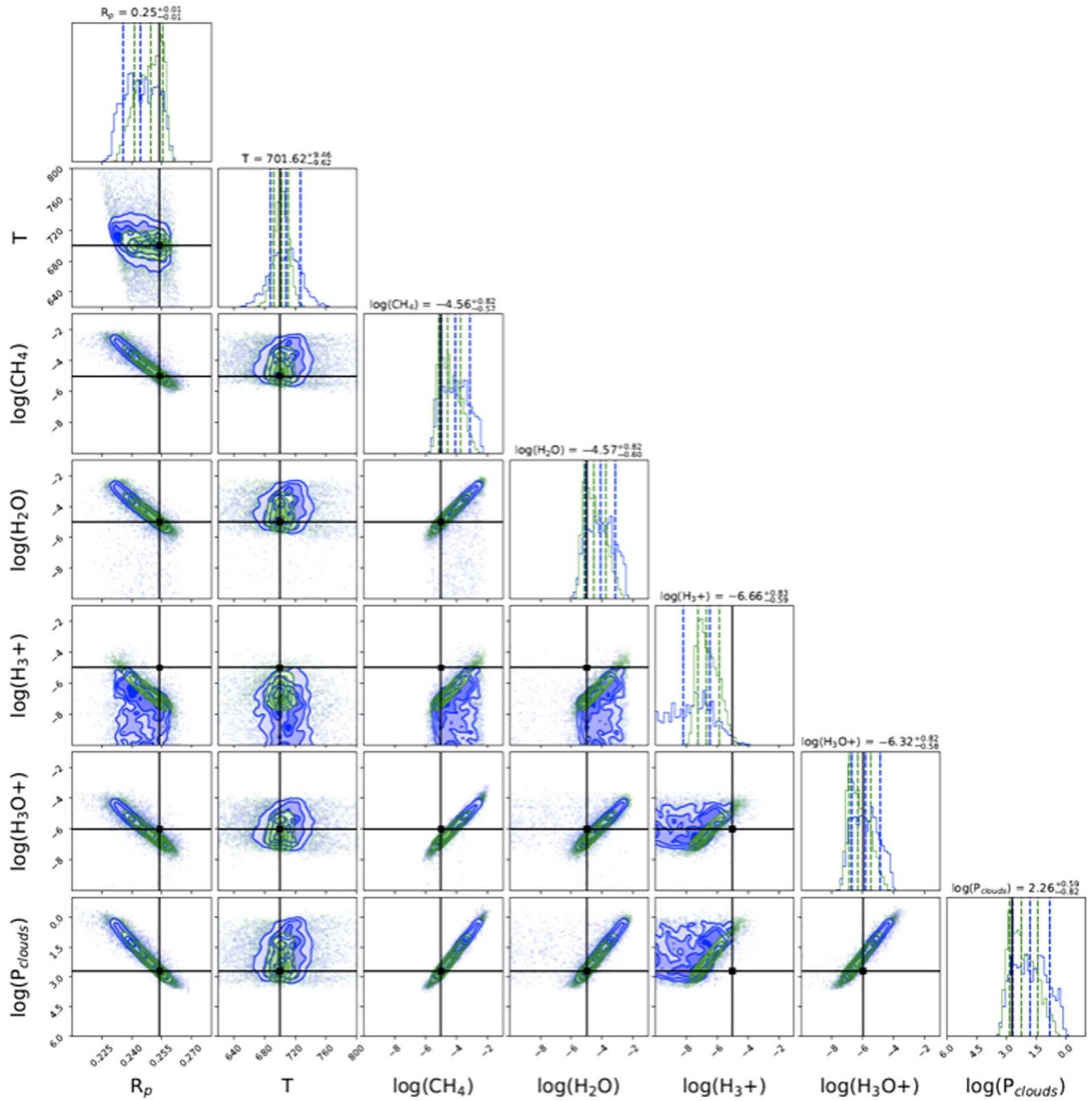


**Figure 7.** Posterior distributions for ARIEL (blue) and JWST (green) retrievals of our GJ1214b planet case.

features in the wavelength range covered by Ariel and JWST. As there are still few models of exoplanets to incorporate reactions with ions, the abundances of  $\text{H}_3^+$  and  $\text{H}_3\text{O}^+$  that can be expected remain unclear. We present the results with realistic mixing ratios inspired by the work of Helling & Rimmer (2019). The purpose of these simulations was to determine, with the resolution of future telescopes, if these mixing ratios would allow the cations to be detected in the atmospheres of exoplanets and through which transitions. While their profiles may vary with altitude, for the purposes of our simplified example, we consider that they are vertically mixed and hence constant with altitude (see Figure 5).

It should be noted that no object exactly similar to our experimental gas mixtures has yet been identified, but the fact that  $\text{CH}_4$  replaces  $\text{CO}/\text{N}_2$  among the secondary species does

not change the final result, which is that  $\text{H}_3\text{O}^+$  and  $\text{H}_3^+$  will be among the major ions formed in an  $\text{H}_2$ -dominated environment where there is the presence of oxygen, even if only in trace amounts (Hollenbach et al. 2012; Beuther et al. 2014; Gerin et al. 2016). Efficient series of proton transfer reactions from  $\text{H}_3^+$  or other abundant ions, depending on the secondary species in the environments, will easily lead to the formation of  $\text{H}_3\text{O}^+$  (Indriolo & McCall 2013; Van Dishoeck et al. 2013), making the detection of  $\text{H}_3\text{O}^+$  and  $\text{H}_3^+$  in an object like GJ1214b quite legitimate.

In both the ARIEL and JWST cases, our retrieval analysis manages to reproduce the observed spectra (see Figure 6). We can see that  $\text{H}_3\text{O}^+$  is detectable by both instruments (see also posterior distributions Figure 7). Indeed,  $\text{H}_3\text{O}^+$  presents a wide feature around  $2.8 \mu\text{m}$ , which is easily captured. However,  $\text{H}_3^+$

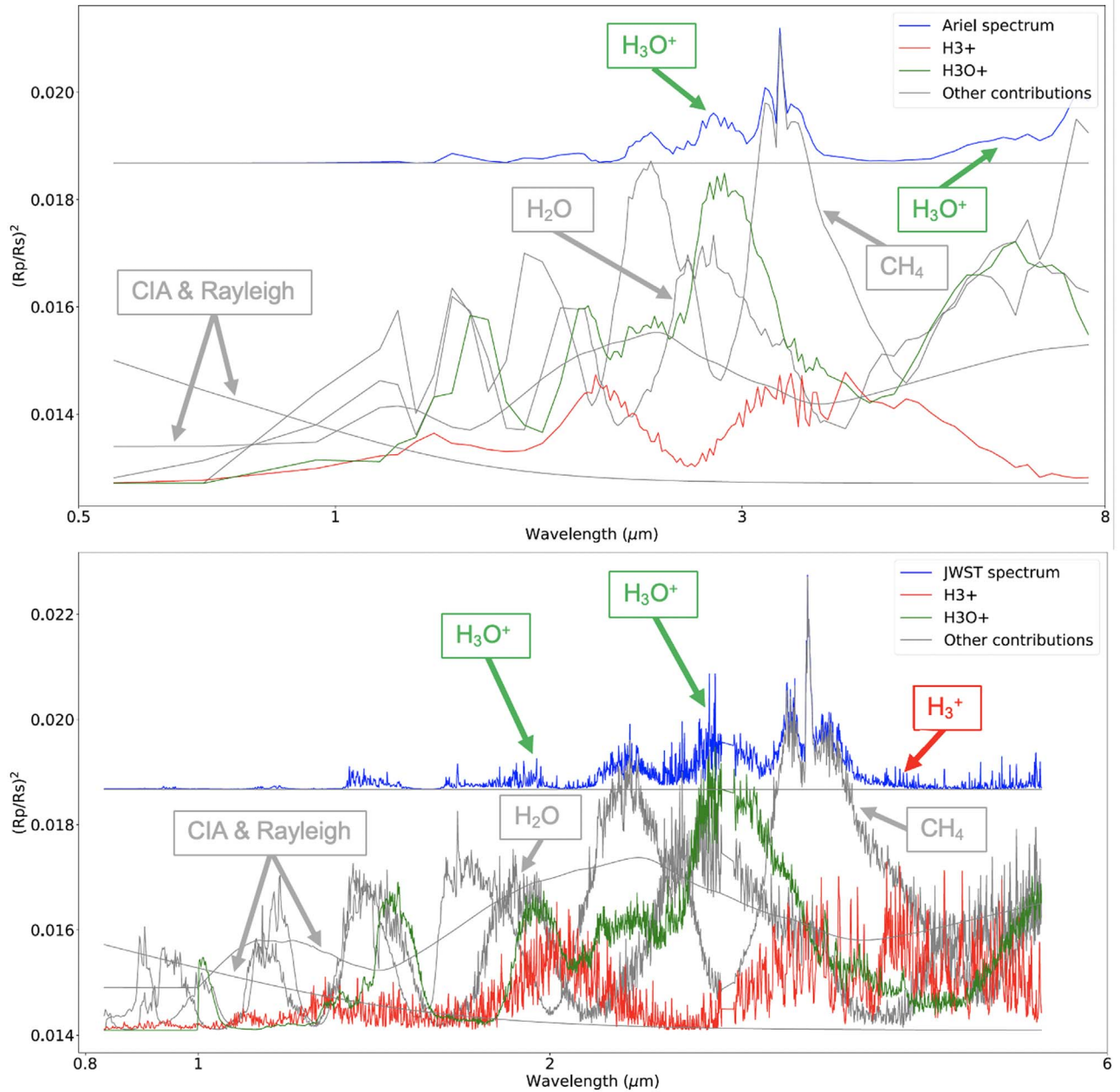


**Figure 8.** Contribution of the different absorbers to the transmission spectra of our best-fit retrievals for ARIEL (top) and JWST (bottom).

exhibits much weaker features that are largely masked by the clouds. In general, the gray cloud cover, which represents a pessimistic assumption, introduces a large degeneracy with the planet radius and the retrieved abundances (see Figure 8). This, along with the assumption of constant chemistry in the retrievals, explains the slight difference from the true and retrieved chemistry for  $\text{H}_2\text{O}$  and  $\text{CH}_4$ . The  $\text{H}_3^+$  is only successfully detected in the JWST simulated spectrum thanks to the presence of small features only seen at high resolution. In the ARIEL case, an upper limit of  $10^{-5}$  on  $\text{H}_3^+$  abundance can be deduced, but the detection remains unclear. In order to detect this ion with ARIEL, higher abundances or a slightly higher number of transits will be necessary.

#### 4. Conclusion

Laboratory experiments simulating thermospheric chemistry in the simplified atmospheres of super-Earth and mini-Neptune exoplanets were performed. A photochemical reactor containing gas mixtures with different mixing ratios of  $\text{H}_2$  and important exoplanetary trace compounds ( $\text{CO}$  and  $\text{N}_2$ ) were irradiated at a pressure of 0.9 mbar, representative of high altitude in an exoplanetary atmosphere, and a wavelength of 73.6 nm. The photoproducted ions were measured using a quadrupole MS, and the experimental data were compared to the expected abundances of a 0D photochemical model. A sensitivity analysis based on the Monte Carlo method allows us to confirm  $\text{H}_3^+$  as one of the main ions in environments rich in  $\text{H}_2$ . Our retrieval analysis based on these simulations shows that in realistic conditions, the next generation of space telescopes should be able to accurately constrain  $\text{H}_3\text{O}^+$

abundances in sub-Neptunes due to the large broadband feature at around  $2.8\ \mu\text{m}$ . For  $\text{H}_3^+$ , the strongest features seem to require high resolution, which can easily be achieved by JWST but would require the stacking of a large number of observations in the case of ARIEL. Even if the presence of other molecules makes detections more difficult, spectral retrieval models provide a powerful technique to disentangle the contribution of the different species from the data (Gandhi & Madhusudhan 2017; Goyal et al. 2017; Lavie et al. 2017; Lammer et al. 2019). Additionally,  $\text{H}_3^+$  is very reactive and tends to donate a proton to all of the molecules it encounters, enriching the chemistry through chain reactions to form more complex and diverse molecules. Thus,  $\text{H}_3^+$  will be difficult to observe if it reacts very quickly with neighboring molecules such as CO and  $\text{N}_2$ , as shown in this work. Given the results of this work, we suggest that it should be fruitful to search upper exoplanetary atmospheres for abundant protonated ions, such as  $\text{H}_3\text{O}^+$ , produced by reactions with  $\text{H}_3^+$ . The simultaneous detection of  $\text{H}_3^+$  and  $\text{H}_3\text{O}^+$  ions would serve to constrain the parameters when characterizing exoplanets.

Several future ground- and space-based telescopes (JWST, ARIEL, E-ELT, TMT) will allow the characterization of the atmospheres of exoplanets using IR spectroscopy, in particular to search for biosignatures within the atmospheres of rocky planets. Cool stars, such as M dwarfs, are preferred targets for the search for rocky temperate planets, as they have a closer habitable zone due to their size and temperature that favors the detection and characterization of terrestrial exoplanets (Scalo et al. 2007; Tarter et al. 2007). However, the exposure of planetary atmospheres to the strong UV radiation from these active stars may have a drastically negative effect on the habitability of planets (Tian 2009; Erkaev et al. 2013; Miguel et al. 2014; Luger & Barnes 2015; Chadney et al. 2016). High-energy radiation drives the chemical composition, including the formation of IR-radiating species that will influence the evolution of the atmosphere by controlling its thermal structure. Species like  $\text{H}_3^+$  and  $\text{H}_3\text{O}^+$  with different cooling rates will allow different EUV responses to thermospheric expansion and hinder the escape of atoms and other volatiles that could be required for life. Thus, the detection of these ions can provide information on the physical parameters of atmospheres and the formation of atmospheric constituents. For instance, the saturated molecular hydronium ion is known to play an important role in the planetary and interstellar oxygen chemistry network in a way that dissociative recombination of hydronium ions with electrons could be a source of target molecules related to habitability, like water vapor and  $\text{O}_2$  (Larsson & Orel 2008). Thus,  $\text{H}_3^+$  or  $\text{H}_3\text{O}^+$  may be used to estimate water vapor and  $\text{O}_2$  abundances when direct detection is unfeasible.

As a conclusion, this work proposed  $\text{H}_3^+$  and  $\text{H}_3\text{O}^+$  as potential tracers of the nature and evolution of low-gravity exoplanets. Formation of  $\text{H}_3^+$  is negligible in low- $\text{H}_2$  environments but important in  $\text{H}_2$ -rich gas mixtures, while  $\text{H}_3\text{O}^+$  should remain abundant in both environments if water vapor is present in the atmosphere, even at a trace level. Thus, nondetection of  $\text{H}_3^+$  associated with the observation of  $\text{H}_3\text{O}^+$  in an exoplanetary atmosphere would provide additional information for the classification of planets in the transition between super-Earths and mini-Neptunes.

Future studies should focus on the potential detection of the other major ions highlighted in this work,  $\text{HCO}^+$  and  $\text{N}_2\text{H}^+$ ,

which may be relatively abundant within the atmospheres of exoplanets where CO and  $\text{N}_2$  would be present. However, theoretical calculations are required to provide a list of absorption transitions and their related intensities for these species. One strategy to support the theoretical calculations would be to develop experimental devices to measure ion absorption cross sections in the IR. Experimental devices must begin to focus on the evolution of thermospheric chemistry as a function of temperature, which requires the development of simulation chambers that can be temperature-controlled between 300 and 1000 K. Finally, photochemical models of exoplanets should begin to take into account the coupling between the chemistry of neutral species and ions for the simulation of atmospheres of cold and warm exoplanets.

This research was supported by the European Research Council Starting Grant PRIMCHEM 636829 to N.C. O.V. thanks the CNRS/INSU Programme National de Planétologie (PNP) and the CNES for funding support. We acknowledge the help of and fruitful discussions with Dr. Billy Edwards, who provided access to his JWST noise simulator ExoWebb.

### ORCID iDs

Jérémy Bourgalais  <https://orcid.org/0000-0003-4710-8943>  
 Nathalie Carrasco  <https://orcid.org/0000-0002-0596-6336>  
 Quentin Changeat  <https://orcid.org/0000-0001-6516-4493>  
 Olivia Venot  <https://orcid.org/0000-0003-2854-765X>  
 Jonathan Tennyson  <https://orcid.org/0000-0002-4994-5238>  
 Sergey N. Yurchenko  <https://orcid.org/0000-0001-9286-9501>  
 Giovanna Tinetti  <https://orcid.org/0000-0001-6058-6654>

### References

- Abel, M., Frommhold, L., Li, X., & Hunt, K. L. 2011, *JPCA*, **115**, 6805  
 Abel, M., Frommhold, L., Li, X., & Hunt, K. L. 2012, *JChPh*, **136**, 044319  
 Barber, R. J., Miller, S., Dello Russo, N., et al. 2009, *MNRAS*, **398**, 1593  
 Barton, E. J., Hill, C., Yurchenko, S. N., et al. 2017, *JQSRT*, **187**, 453  
 Beuther, H., Klessen, R. S., Dullemond, C. P., & Henning, T. K. 2014, *Protostars and Planets VI* (Tucson, AZ: Univ. Arizona Press)  
 BIPM/IEC/FCC et al. 2008, Evaluation of Measurement Data—Supplement 1 to the “Guide to the expression of uncertainty in measurement”—Propagation of distributions using a Monte Carlo method, Tech. Rep., 101:2008, Joint Committee for Guides in Metrology, JCGM [http://www.bipm.org/utis/common/documents/jcgm/JCGM\\_101\\_2008\\_E.pdf](http://www.bipm.org/utis/common/documents/jcgm/JCGM_101_2008_E.pdf)  
 Bolmont, E., Selsis, F., Owen, J. E., et al. 2016, *MNRAS*, **464**, 3728  
 Borucki, W. J. 2016, *RPPh*, **79**, 036901  
 Bourgalais, J., Carrasco, N., Vettier, L., & Pernot, P. 2019, *JGRA*, **124**, 9214  
 Bourrier, V., Ehrenreich, D., Wheatley, P., et al. 2017, *A&A*, **599**, L3  
 Carrasco, N., Alcaraz, C., Dutuit, O., et al. 2008, *P&SS*, **56**, 1644  
 Carrasco, N., Giuliani, A., Correia, J.-J., & Cernogora, G. 2013, *Journal of Synchrotron Radiation*, **20**, 587  
 Chabrier, G. 2003, *PASP*, **115**, 763  
 Chadney, J., Galand, M., Koskinen, T., et al. 2016, *A&A*, **587**, A87  
 Chadney, J., Galand, M., Unruh, Y., Koskinen, T., & Sanz-Forcada, J. 2015, *Icar*, **250**, 357  
 Changeat, Q., Edwards, B., Waldmann, I., & Tinetti, G. 2019, *ApJ*, **886**, 39  
 Coughlin, J. L., Mullally, F., Thompson, S. E., et al. 2016, *ApJS*, **224**, 12  
 Dobrijevic, M., Loison, J., Hickson, K., & Gronoff, G. 2016, *Icar*, **268**, 313  
 Drummond, B., Tremblin, P., Baraffe, I., et al. 2016, *A&A*, **594**, A69  
 Dubois, D., Carrasco, N., Petrucci, M., et al. 2019, *Icar*, **317**, 182  
 Elkins-Tanton, L. T., & Seager, S. 2008, *ApJ*, **685**, 1237  
 Erkaev, N. V., Lammer, H., Odert, P., et al. 2013, *AsBio*, **13**, 1011  
 Feng, Y. K., Robinson, T. D., Fortney, J. J., et al. 2018, *AJ*, **155**, 200  
 Feroz, F., Gair, J. R., Hobson, M. P., & Porter, E. K. 2009, *CQGrA*, **26**, 215003  
 Fletcher, L. N., Gustafsson, M., & Orton, G. S. 2018, *ApJS*, **235**, 24  
 France, K., Loyd, R. P., Youngblood, A., et al. 2016, *ApJ*, **820**, 89  
 Gandhi, S., & Madhusudhan, N. 2017, *MNRAS*, **474**, 271

- Gans, B., Mendes, L. A. V., Boyé-Péronne, S., et al. 2010, *JPCA*, **114**, 3237
- Gao, P., Hu, R., Robinson, T. D., Li, C., & Yung, Y. L. 2015, *ApJ*, **806**, 249
- Gardner, J. P., Mather, J. C., Clampin, M., et al. 2006, *SSRv*, **123**, 485
- Geballe, T., Jagod, M.-F., & Oka, T. 1993, *ApJL*, **408**, L109
- Gerin, M., Neufeld, D. A., & Goicoechea, J. R. 2016, *ARA&A*, **54**, 181
- Goicoechea, J. R., & Cernicharo, J. 2001, *ApJL*, **554**, L213
- Gordon, I., Rothman, L. S., Wilzewski, J. S., et al. 2016, AAS/DPS Meeting Abstracts, **48**, 421.13
- Goyal, J. M., Mayne, N., Sing, D. K., et al. 2017, *MNRAS*, **474**, 5158
- Harpsoe, K. B. W., Hardis, S., Hinse, T., et al. 2013, *A&A*, **549**, A10
- He, C., Hörst, S. M., Lewis, N. K., et al. 2018a, *ApJL*, **856**, L3
- He, C., Hörst, S. M., Lewis, N. K., et al. 2018b, *AJ*, **156**, 38
- He, C., Hörst, S. M., Lewis, N. K., et al. 2019, *ESC*, **3**, 39
- Heays, A., Bosman, A. D. v., & Van Dishoeck, E. 2017, *A&A*, **602**, A105
- Hébrard, E., Dobrijevic, M., Bénilan, Y., & Raulin, F. 2006, *Journal of Photochemistry and Photobiology C: Photochemistry Reviews*, **7**, 211
- Hébrard, E., Dobrijevic, M., Pernot, P., et al. 2009, *JPCA*, **113**, 11227
- Helling, C., & Rimmer, P. B. 2019, *RSPTA*, **377**, 20180398
- Hill, C., Yurchenko, S. N., & Tennyson, J. 2013, *Icar*, **226**, 1673
- Hollenbach, D., Kaufman, M., Neufeld, D., Wolfire, M., & Goicoechea, J. 2012, *ApJ*, **754**, 105
- Hörst, S. M. 2017, *JGRE*, **122**, 432
- Hörst, S. M., He, C., Lewis, N. K., et al. 2018, *NatAs*, **2**, 303
- Hu, R. 2015, in *Planetary Exploration and Science: Recent Results and Advances* (Berlin: Springer), 291
- Hu, R., & Seager, S. 2014, *ApJ*, **784**, 63
- Huebner, W., & Mukherjee, J. 2015, *P&SS*, **106**, 11
- Indriolo, N., & McCall, B. J. 2013, *ChSRv*, **42**, 7763
- Jontof-Hutter, D. 2019, *AREPS*, **47**, 141
- Kempton, E. M.-R., Zahnle, K., & Fortney, J. J. 2011, *ApJ*, **745**, 3
- Koskinen, T., Aylward, A., Smith, C., & Miller, S. 2007, *ApJ*, **661**, 515
- Koskinen, T., Harris, M., Yelle, R., & Lavvas, P. 2013, *Icar*, **226**, 1678
- Koskinen, T., Yelle, R., Lavvas, P., & Lewis, N. 2010, *ApJ*, **723**, 116
- Kreidberg, L., Bean, J. L., Désert, J.-M., et al. 2014, *Natur*, **505**, 69
- Lammer, H., Eybl, V., Kislyakova, K., et al. 2011, *Ap&SS*, **335**, 39
- Lammer, H., Sproß, L., Grenfell, J. L., et al. 2019, *AsBio*, **19**, 927
- Larsson, M., & Orel, A. E. 2008, *Dissociative Recombination of Molecular Ions* (Cambridge: Cambridge Univ. Press)
- Laughlin, G., Bodenheimer, P., & Adams, F. C. 2004, *ApJL*, **612**, L73
- Lavie, B., Mendonça, J. M., Mordasini, C., et al. 2017, *AJ*, **154**, 91
- Lavvas, P., Koskinen, T., & Yelle, R. V. 2014, *ApJ*, **796**, 15
- Lenz, L., Reiners, A., Seifahrt, A., & Käufel, H.-U. 2016, *A&A*, **589**, A99
- Loyd, R. P., France, K., Youngblood, A., et al. 2016, *ApJ*, **824**, 102
- Luger, R., & Barnes, R. 2015, *AsBio*, **15**, 119
- Melnikov, V. V., Yurchenko, S. N., Tennyson, J., & Jensen, P. 2016, *PCCP*, **18**, 26268
- Miguel, Y., Kaltenecker, L., Linsky, J. L., & Rugheimer, S. 2014, *MNRAS*, **446**, 345
- Miller, S., Rego, D., Achilleos, N., et al. 2000, *AdSpR*, **26**, 1477
- Miller, S., Stallard, T., Melin, H., & Tennyson, J. 2010, *FaDi*, **147**, 283
- Miller, S., Stallard, T., Tennyson, J., & Melin, H. 2013, *JPCA*, **117**, 9770
- Mizus, I. I., Aljiah, A., Zobov, N. F., et al. 2017, *MNRAS*, **468**, 1717
- Moran, S., Horst, S., Vuitton, V., et al. 2020, arXiv:2004.13794
- Morley, C. V., Fortney, J. J., Kempton, E. M.-R., et al. 2013, *ApJ*, **775**, 33
- Moses, J. I., Line, M. R., Visscher, C., et al. 2013, *ApJ*, **777**, 34
- Moses, J. I., Visscher, C., Fortney, J. J., et al. 2011, *ApJ*, **737**, 15
- Mugnai, L., Edwards, B., Papageorgiou, A., Pascale, E., & Sarkar, S. 2019, EPSC-DPS Joint Meeting, 2019, 13
- Muñoz, A. G. 2007, *P&SS*, **55**, 1426
- Neale, L., Miller, S., & Tennyson, J. 1996, *ApJ*, **464**, 516
- Owen, J. E., & Mohanty, S. 2016, *MNRAS*, **459**, 4088
- Peng, Z., Carrasco, N., & Pernot, P. 2014, *GeoResJ*, **1**, 33
- Pierrehumbert, R., & Gaidos, E. 2011, *ApJL*, **734**, L13
- Plessis, S., Carrasco, N., Dobrijevic, M., & Pernot, P. 2012, *Icar*, **219**, 254
- Polyansky, O. L., Kyuberis, A. A., Zobov, N. F., et al. 2018, *MNRAS*, **480**, 2597
- Ribas, I., Bolmont, E., Selsis, F., et al. 2016, *A&A*, **596**, A111
- Rimmer, P. B., & Helling, C. 2016, *ApJS*, **224**, 9
- Rimmer, P. B., & Rugheimer, S. 2019, *Icar*, **329**, 124
- Rimmer, P. B., Xu, J., Thompson, S. J., et al. 2018, *SciA*, **4**, eaar3302
- Rothman, L. S., Gordon, I. E., Barber, R. J., et al. 2010, *JQSRT*, **111**, 2139
- Scalo, J., Kaltenecker, L., Segura, A., et al. 2007, *AsBio*, **7**, 85
- Schaefer, L., Lodders, K., & Fegley, B. 2012, *ApJ*, **755**, 41
- Shampine, L. F., Sommeijer, B. P., & Verwer, J. G. 2006, *JCoAM*, **196**, 485
- Shkolnik, E., Gaidos, E., & Moskovitz, N. 2006, *AJ*, **132**, 1267
- Shkolnik, E. L., & Barman, T. S. 2014, *AJ*, **148**, 64
- Stallard, T., Miller, S., Millward, G., & Joseph, R. D. 2001, *Icar*, **154**, 475
- Tarter, J. C., Backus, P. R., Mancinelli, R. L., et al. 2007, *AsBio*, **7**, 30
- Tennyson, J., Yurchenko, S. N., Al-Refai, A. F., et al. 2016, *JMoSp*, **327**, 73
- Tian, F. 2009, *ApJ*, **703**, 905
- Tigrine, S., Carrasco, N., Vettier, L., & Cernogora, G. 2016, *JPhD*, **49**, 395202
- Tinetti, G., Drossart, P., Eccleston, P., et al. 2016, *Proc. SPIE*, **9904**, 99041X
- Tinetti, G., Drossart, P., Eccleston, P., et al. 2018, *ExA*, **46**, 135
- Trafton, L. M., Geballe, T., Miller, S., Tennyson, J., & Ballester, G. 1993, *ApJ*, **405**, 761
- Van Dishoeck, E. F., Herbst, E., & Neufeld, D. A. 2013, *ChRv*, **113**, 9043
- Venot, O., Agúndez, M., Selsis, F., Tessenyi, M., & Iro, N. 2014, *A&A*, **562**, A51
- Verwer, J. G., & Sommeijer, B. P. 2004, *SIAM Journal on Scientific Computing*, **25**, 1824
- Vuitton, V., Yelle, R., Klippenstein, S., Hörst, S., & Lavvas, P. 2019, *Icar*, **324**, 120
- Wakelam, V., Herbst, E., Loison, J.-C., et al. 2012, *ApJS*, **199**, 21
- Waldmann, I. P., Rocchetto, M., Tinetti, G., et al. 2015a, *ApJ*, **813**, 13
- Waldmann, I. P., Tinetti, G., Rocchetto, M., et al. 2015b, *ApJ*, **802**, 107
- Wolters, C., Vuitton, V., Flandinet, L., et al. 2019, EPSC, **13**, 2029
- Wordsworth, R., & Pierrehumbert, R. 2014, *ApJL*, **785**, L20
- Yelle, R. V. 2004, *Icar*, **170**, 167
- Youngblood, A., France, K., Loyd, R. P., et al. 2016, *ApJ*, **824**, 101
- Yurchenko, S. N., Tennyson, J., Bailey, J., Hollis, M. D., & Tinetti, G. 2014, *PNAS*, **111**, 9379
- Yurchenko, S. N., Tennyson, J., Miller, S., et al. 2020, *MNRAS*, submitted